

Gradient-based optimization of scatterer arrangements based on the T-Matrix method

N. Asadova,¹ J.D. Fischbach,¹ R. Vallée,² Y. Augenstein,³ D. Vovchuk,^{4,5} A. Kharchevskii,⁵ P. Ginzburg,⁵ and C. Rockstuhl^{1,6,7}

¹⁾*Institute of Nanotechnology, Karlsruhe Institute of Technology (KIT), Karlsruhe, Germany*

²⁾*Centre de Recherche Paul Pascal, University of Bordeaux, Pessac, France*

³⁾*Flexcompute Inc, Belmont, MA, USA*

⁴⁾*Institute of Photonics, Electronics and Telecommunications, Riga Technical University, Riga, Latvia*

⁵⁾*School of Electrical Engineering, Tel Aviv University, Tel Aviv, Israel*

⁶⁾*Institute of Theoretical Solid State Physics, Karlsruhe Institute of Technology (KIT), Karlsruhe, Germany*

⁷⁾*Center for Integrated Quantum Science and Technology (IQST), Karlsruhe Institute of Technology (KIT), Karlsruhe, Germany*

(*Electronic mail: nigar.asadova@kit.edu)

The demand for inverse design is increasing as the ability to fabricate sub-10 nm features expands the design space by orders of magnitude. Efficient inverse design benefits from differentiable models of light-structure interaction. While traditional full-wave solvers based on finite differences, finite elements, or Fourier modal methods have already been presented for that purpose, a dedicated tool adapted for performing multiple scattering simulations is still lacking. To overcome this limitation, we provide a multiple-scattering framework compatible to automatic differentiation, suitable for treating periodic and non-periodic arrangements of scatterers. It yields exact gradients regarding geometric and positional parameters in finite clusters and infinite metasurfaces. In this work, we use spheres as the elementary building blocks to demonstrate the framework's capabilities as a standalone tool. However, the framework is adaptable to arbitrarily shaped scatterers, provided the individual T-matrices are calculated using differentiable full-wave Maxwell solvers. Since the gradients are obtained simultaneously in a single backward pass, the framework is well-suited for moderately dimensional problems. It is also possible to combine multiple performance goals into a single objective function. The versatility of our method is illustrated in proof-of-concept examples that focus on various aspects of Kerker-type physics. In the first example, a finite cluster of scatterers is optimized in order to reach a high forward-to-backward scattering ratio, and we show experimental feasibility of the designs. In the second example, a metasurface made from multiple scatterers in each unit cell is designed to maximize the reflectance contrast between orthogonal linear polarizations of the incident light. We make the framework publicly available at <https://github.com/tfp-photonics/dreams>.

I. INTRODUCTION

With recent advances in the fabrication of nanophotonic devices, numerous design parameters can be tailored to achieve a desired optical response. This increase in degrees of freedom necessitates solving the inverse problem efficiently. In other words, we need to identify optimal design parameters so the nanophotonic device exhibits the desired optical response.

The most basic approach is to perform a parameter sweep and select the best performance among the calculated objective values. However, this quickly becomes infeasible with an increasing number of parameters, a phenomenon known as the curse of dimensionality. Therefore, over the decades, a plethora of more advanced approaches were introduced^{1–5}. The problem to be solved within the framework of inverse design is to adjust each degree of freedom to reach the optimum for a desired objective function. Inverse design employs various strategies such as deep learning^{6,7}, topology optimization^{8,9}, metaheuristic algorithms^{10–12}, or probabilistic algorithms^{13,14}.

However, scalability remains a critical challenge^{15,16}. As the number of design parameters increases, the computational time required by heuristic methods often increases exponen-

tially, making them less suitable for high-dimensional design problems¹⁷. Among different approaches, deep learning models provide practically immediate results after the training phase is completed. However, training depends on the availability of an extensive dataset. The data generation process scales exponentially with the dimensionality of the design space¹⁸, and in the majority of cases, each particular problem requires a dedicated training set. This renders such approaches computationally expensive in scenarios where the training data must be explicitly generated solely to train a neural network to solve a specific inverse design problem.

Therefore, in high-dimensional parameter spaces, gradient-based optimization methods are the primary choice for solving inverse problems. The known gradients provide the shortest path to a local optimum. Although the optimum is not global, the curse of dimensionality can become a blessing¹⁹. For very high-dimensional parameter spaces, the landscape is expected to flatten out such that the local maximum or minimum is close in value to the global one. However, this effect depends on the specific nature of the problem and must be empirically tested.

The calculation of gradients for complex computational code can be implemented in different ways. Numerical implementation with finite differences is typically not consid-

ered, since it requires performing one additional simulation for each parameter variation. In the adjoint method, a second problem has to be manually formulated and solved, and the solution provides the gradient of the objective function. It is usually formulated for PDE problems. The adjoint method is extensively used in topology optimization, where each pixel or voxel in the device elements serves as a degree of freedom²⁰. This easily amounts to a total of 10^3 - 10^9 degrees of freedom. The resulting optimized shapes are free-form, and potential fabrication difficulties should be handled as well²¹⁻²³.

An alternative approach to obtaining gradients is automatic differentiation (AD) – an automated approach that evaluates exact derivatives of a composition of elementary functions. As it takes the same amount of time to calculate the derivative with respect to all parameters, regardless of the number of parameters, a single optimization step takes roughly twice the time of a single simulation. Hybrid approaches replace manual derivation of the adjoint equation with AD²⁴. However, fully differentiable implementations go further, re-implementing the solver entirely within a framework with AD capabilities for ease of use and high performance.

Formulating tools for scientific computations in an automatically differentiable manner requires dedicated effort and careful implementation. In essence, every elementary function needs to be formulated as differentiable, something which poses challenges. Nevertheless, with the appreciation that gradient information is key to inverse design in high-dimensional parameter spaces, multiple efforts have been dedicated to formulating various methods that solve Maxwell's equations in an automatically differentiable manner. These include general-purpose full-wave Maxwell solvers, such as the finite-difference time-domain (FDTD) method^{25,26}, the finite element method (FEM)^{27,28}, and others.

A special-purpose computational method that was already formulated in an automatically differentiable manner is the rigorous coupled-wave analysis (RCWA) method, also known as the Fourier modal method (FMM)^{29,30}. It has been extensively used within the AD framework³¹⁻³⁵ or adjoint method³⁶, and can be combined with topology optimization^{9,37}. Another semi-analytical approach with a recently developed differentiable implementation is the hybrid coupled dipole method³⁸. However, each of these automatically differentiable formulations inherits the pros and cons of the underlying computational method. Therefore, having a wide range of tools available that can be flexibly applied to specific problems is highly beneficial for further developing nanophotonics.

This contribution focuses on the automatic differentiation of a computational framework for nanophotonic scattering problems based on the T-matrix method. The benefit of the method lies in its semi-analytical treatment of the light-matter interaction with the elementary building blocks expressed using the T-matrix. The T-matrix captures how an incident field, expanded into vector spherical waves, is converted into a scattered field, which is also expanded into vector spherical waves. Once the T-matrix of an object is known, complex arrangements of many scatterers can be studied highly efficiently based on an underlying algebraic formulation. The

scatterers can be arranged randomly or in a periodic pattern, forming metasurfaces or metamaterials. Such versatility renders the T-matrix applicable to a wide range of nanophotonic problems³⁹⁻⁴². Our implementation follows the open-source *dreams* package⁴³ and integrates AD capabilities into the multiscattering code.

A central milestone of our work is the development of a differentiable computational framework for calculating the optical response of complex arrangements of scatterers. The framework that we develop here enables differentiation with respect to input parameters, including not only the radii of individual spheres but also the positions of spheres or arbitrarily shaped scatterers in arrangements such as periodic arrays with complex unit cells containing multiple scatterers.

Earlier implementations used analytically calculated derivatives of Mie coefficients, and the final derivatives were obtained using the adjoint method^{44,45}. These works did not utilize the AD framework, and the parametrization of scatterer positions was not integrated, as it requires more manual derivations. Recent publications applied gradient-free optimization to infinitely extended core-shell cylinders⁴⁶ and the arrangement of spheres⁴⁷. Gradient-based optimization for chains of infinite cylinders was performed with Gaussian parameterization of positions⁴⁸.

The article is structured as follows. In Section II, the multiscattering formalism is introduced, and the fundamentals of AD are outlined. In Section III, an arrangement of spheres is optimized to achieve the maximum scattering ratio between the forward and backward hemispheres. Next, the optimization results for an example of a metasurface with a complex unit cell composed of spheres, optimized for polarization-selective reflectance, are discussed. By making the underlying Python source codes developed in this work publicly available on GitHub (<https://github.com/tfp-photonics/dreams>), we expect a substantial contribution to the further development of the field of nanophotonics that relies on scattering structures.

II. AUTOMATIC DIFFERENTIATION OF MULTISCATTERING FRAMEWORK

A. Multiscattering formalism

The T-matrix formalism is a versatile approach that simplifies the computation of the optical response for various arrangements of scatterers. Here, the T-matrix represents the linear relationship between expansion coefficients of the regular vector spherical waves that expand the incident field and the singular vector spherical waves that expand the scattered field:

$$\mathbf{p} = \mathbf{T} \mathbf{a}. \quad (1)$$

p and **a** are vectors containing the expansion coefficients for the scattered field and the incident field, respectively:

$$\mathbf{E}_{\text{inc}}(\mathbf{r}, \omega) = \sum_{l=1}^{\infty} \sum_{m=-l}^l \left[a_{lm}^{\text{e}}(\omega) \mathbf{N}_{lm}^{(1)}(\mathbf{r}, \omega) + a_{lm}^{\text{m}}(\omega) \mathbf{M}_{lm}^{(1)}(\mathbf{r}, \omega) \right] \quad (2)$$

$$\mathbf{E}_{\text{sca}}(\mathbf{r}, \omega) = \sum_{l=1}^{\infty} \sum_{m=-l}^l \left[p_{lm}^{\text{e}}(\omega) \mathbf{N}_{lm}^{(3)}(\mathbf{r}, \omega) + p_{lm}^{\text{m}}(\omega) \mathbf{M}_{lm}^{(3)}(\mathbf{r}, \omega) \right] \quad (3)$$

The fields are expanded in transverse electric (TE) and transverse magnetic (TM) vector spherical waves $\mathbf{M}_{lm}(\mathbf{r}, \omega)$ and $\mathbf{N}_{lm}(\mathbf{r}, \omega)$. The superscripts correspond to regular (1) and singular (3) fields⁴⁹. The T-matrix \mathbf{T} represents the most comprehensive information on the linear optical response of a scatterer and can be obtained semi-analytically for basic objects, e.g., spheres, or numerically for arbitrarily shaped scatterers.

The number of multipolar orders in the expansion can be truncated at a specific value, beyond which the contribution to the optical response can be considered negligible. This approach, therefore, offers clear advantages over the commonly used dipole approximation.

For arrangements of scatterers, a modified expression holds that accounts for the contribution of the scattered field coming from other scatterers to the incident field on each scatterer:

$$\mathbf{p} = (\mathbf{1} - \mathbf{T}\mathbf{C}^{(3)})^{-1} \mathbf{T}\mathbf{a}, \quad (4)$$

where \mathbf{T} is a block-diagonal matrix where each scatterer response is defined in its local coordinate system. All the translation coefficients are packed in the matrix $\mathbf{C}^{(3)}$, and $\mathbf{C}_{ij}^{(3)}$ depends on the distance from the j -th scatterer to the i -th scatterer. Please note that this is what we refer to as a local description, as each scatterer is represented by its T-matrix.

We can also employ a global T-matrix formulation, where the entire scattering response of an ensemble of scatterers is expressed relative to a specific origin^{50,51}. This is beneficial since the T-matrix shrinks in size for problems with closely arranged scatterers. For the scattering problem of a periodic lattice, $\mathbf{C}_{ij}^{(3)}$ includes a sum over an infinite number of lattice sites. The direct evaluation of the sum converges poorly, so the Ewald method is employed^{52,53}. By expanding the resulting T-matrix from the periodic spherical wave basis into the plane wave basis, the S-matrix of a single layer can be obtained that relates the incoming and outgoing plane waves. Finally, the single infinite layer can be stacked with another two-dimensional lattice, an interface, or a homogeneous slab. Thus, the complete framework can simulate a diverse set of scattering arrangements.

B. Automatic differentiation

Now, with this framework, we can express the optical response of various types of photonic materials composed of an ensemble of isolated scatterers. But for the inverse problem, we need to calculate the gradients, i.e., the change of an

objective function derived from a forward simulation, depending on any of the degrees of freedom that we consider. To do so, we will automatically differentiate the code that solves the forward problem.

The basic idea of AD is to apply the chain rule to numerical values and not symbolic expressions. Consider $f : \mathbb{R}^m \rightarrow \mathbb{R}^n$ having m input values and n output values as a sequence of elementary operations. In an optimization task, the derivative of each output with respect to each input variable is required, which makes up a Jacobian of the size $n \times m$. Each intermediate variable in the calculation can be associated with a derivative. Exact derivatives are known for each primitive function. They are linked according to the chain rule, so that the derivative of the function output with respect to an input variable can be easily traced. The order in which the chain rule is applied is what sets apart forward and reverse mode⁵⁴.

In the forward mode, the chain of derivatives is calculated along with the tracing of the function. The Jacobian is not instantiated but defined as a JVP (Jacobian vector product) function that acts on the previous vector by multiplying it from the left. A JVP is formulated as:

$$\text{JVP}(\mathbf{f}(\mathbf{v}, \mathbf{x})) = \frac{\partial \mathbf{f}}{\partial \mathbf{x}} \mathbf{v}(\mathbf{x}), \quad (5)$$

where $\frac{\partial \mathbf{f}}{\partial \mathbf{x}}$ is the Jacobian specified above, and $\mathbf{v}(\mathbf{x})$ is a vector of incoming variables. To find the Jacobian using the forward mode, the following evaluation should start from the right, as indicated by the brackets:

$$\frac{\partial \mathbf{f}}{\partial \mathbf{x}} = \frac{\partial \mathbf{f}}{\partial \mathbf{c}} \left(\frac{\partial \mathbf{c}}{\partial \mathbf{b}} \left(\frac{\partial \mathbf{b}}{\partial \mathbf{a}} \left(\frac{\partial \mathbf{a}}{\partial \mathbf{x}} \mathbf{v} \right) \right) \right), \quad (6)$$

where \mathbf{v} represents one of the basis vectors for the input, filled with 1 in a single entry and 0 in all the other entries, called a one-hot vector. By proceeding as described, one obtains a column of the final Jacobian in one pass, which comprises the derivatives of all outputs with respect to one input. The forward mode is computationally efficient when $m < n$, i.e., the number of inputs is less than the number of outputs.

For many real-world optimization tasks, the output is typically a single value, while the input comprises a considerably larger number of variables. Therefore, it is more advantageous to compute a row of the Jacobian at a time, which includes derivatives of a single output value with respect to all of the inputs. The vector Jacobian product (VJP) is defined as:

$$\text{VJP}(\mathbf{f}(\mathbf{v}, \mathbf{x})) = \mathbf{v}^T \frac{\partial \mathbf{f}}{\partial \mathbf{x}}(\mathbf{x}). \quad (7)$$

Importantly, one should keep in mind that, compared to the forward mode, where the calculation of the gradients is done in parallel, intermediate results have to be stored before starting the backward pass to evaluate the gradients. This results in higher memory consumption. Reverse mode AD is similar to the adjoint method mentioned earlier, while the latter does not assume a fully automatic process, rather a derivation and embedding of the adjoint equations is required. However, even for the simplified automatic differentiation process, there are

numerous pitfalls to be aware of⁵⁵. For a detailed overview of differentiable programming, we refer the reader to a recent review⁵⁶.

JAX is used in the current version of the code to perform automatic differentiation⁵⁷. This approach is a combination of operator overloading, similar to PyTorch,⁵⁸, and source code transformation, which is the approach in Tensorflow⁵⁹. JAX also provides an option to define derivatives for custom primitive functions, which was used to integrate special functions required in the T-matrix approach into the computational flow. For example, spherical Bessel and Hankel functions are not defined in JAX, so they are introduced as primitive functions with their Jacobian vector product manually defined. An example of a primitive function definition is provided in Appendix A. While JAX uses single precision by default, we use double precision throughout optimizations to ensure higher numerical accuracy.

In contrast to the original package *treans*, the core functions are modified because the underlying implementation in Cython is not supported directly in the JAX framework, and they have to be transformed into Python functions. We avoid Python loops, which can introduce computational bottlenecks, opting instead for vectorized operations where it is reasonable. The test functions were computed with the original package and the current code to ensure that the different implementations do not introduce numerical discrepancies. We verified that the gradients computed with automatic differentiation in JAX agree with the finite difference approximation.

III. OPTIMIZATION RESULTS

The final computational tools are made publicly available⁶⁰. To demonstrate the general applicability of our approach and ensure consistency, we present two examples from the field of Kerker-physics that highlight its strengths. These examples are intended to be illustrative, and the methodology can be applied to a wide range of other problems. We begin with an example where we inversely design a finite cluster of scatterers, in order to optimize its integrated forward-to-backward scattering ratio. It is followed by an example where a unit cell of a metasurface, consisting of multiple scatterers, is optimized, maximizing its reflectance for a specified polarization.

A. Finite cluster

If the electric and magnetic dipole responses of a scatterer have equal strength and are in phase at a given wavelength, zero dipolar backward scattering (first Kerker condition) is achieved. If they have opposite phase shift, near-zero dipolar forward scattering (second Kerker condition) takes place⁶¹. According to the generalized Kerker effect^{62,63}, higher-order multipoles can be leveraged to achieve zero total backscattering. This, in essence, requires the constructive interference of all scattering contributions from all multipolar orders in the forward direction. In contrast, they destructively interfere in the backward direction. Even more intricate patterns emerge

when specific combinations of multipoles are engineered^{64,65}. Generally, an object with a scattering cross-section exceeding the single-channel regime is called a superscatterer^{66–68}.

In this work, we consider scattering integrated over the entire forward and backward hemispheres rather than at a single direction. Hemispherical (2π) integration is shown to deliver major advantages over single-angle detection, especially for highly anisotropic nanostructures that scatter light into sharp forward or backward lobes. Experimental studies demonstrate that relying on direct or limited-angle measurements can introduce errors of 10% or more, often underestimating or misrepresenting total scattered power^{69–71}. Only 2π integration supports accurate modeling and optimization, crucial for applications like light-trapping and absorption in solar cells^{70,72,73}.

For these reasons, the objective is defined as:

$$\text{FOM} = \frac{\int |E_{\text{sca}}^f|^2 dS^f}{\int |E_{\text{sca}}^b|^2 dS^b}, \quad (8)$$

where E_{sca}^f and E_{sca}^b represent the scattered field values on the surface of the forward and backward hemisphere S^f and S^b . The integrations are performed in the far field. The integrals are evaluated using discrete quadrature method.

We maximize the F/B scattering ratio from a cluster of particles consisting of a finite number of spheres of a given material. The relative position of the spheres and their size are subject to optimization. Computations employ a local basis for each T-matrix without expanding in a global basis. However, for a later discussion of the multipolar contributions to the scattering response of the entire cluster, we resort to a global basis.

To ensure that all optimization problems comply with the necessary constraints, we incorporate them using a nonlinear optimizer. We opt for the method of moving asymptotes (MMA)⁷⁴ as it handles both bounds and nonlinear constraints. The constraints must be differentiable and evaluated at each iteration. The algorithm builds a sequence of convex and separable approximations to both the objective and the nonlinear constraints. We impose the no-overlap condition of adjacent spheres as a nonlinear constraint on the positions of the spheres for both finite and infinite arrangements. This is implemented by evaluating for all sphere pairs the quantity

$$r_i + r_j - d_{ij} + s,$$

where r_i and r_j are the particle radii, $d_{ij} = \|\mathbf{x}_i - \mathbf{x}_j\|_2$ is the Euclidean distance, and $s \geq 0$ is an optional safety margin. The constraint value is taken as the maximum of this quantity over all pairs, and requiring it to remain non-positive guarantees non-overlap.

Additionally, bound constraints specify the maximum and minimum values for the design variables, ensuring that the objective is not evaluated outside permissible limits. Bounds are set on the minimum radii of the spheres to adhere to possible fabrication constraints. Another potential issue for very small spheres is the significance of quantum effects, which

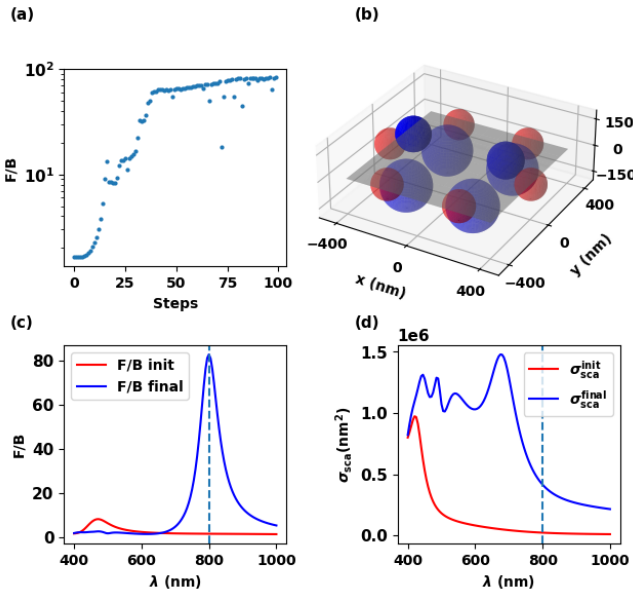


FIG. 1: (a) Convergence of the F/B ratio during optimization at the design wavelength of 800 nm when optimizing the sample from a given initial configuration, as explained in the main text. (b) 3D view of the cluster, with the $z = 0$ plane shown in grey and spheres on the plane rendered with lower transparency. The initial configuration is indicated in red, and the optimized structure in blue. (c) F/B ratio spectrum shows an enhancement at the design wavelength (dashed line). (d) Total scattering cross-section of the initial and final arrangement.

must be accounted for with appropriate approximations. Consequently, we enforce a minimum radius of 5 nm.

For a physically accurate simulation, the maximum radius of the spheres and the minimal distance between them must be consistent with the number of multipoles used. This is ensured by comparing the results against simulations using a higher number of multipoles. For these reasons, we do not restrict the radii to an upper limit. Furthermore, since the local basis formalism is used, it is also not necessary to control whether the distance between spheres becomes too large, which would require more multipoles orders in the global basis expansion than what was sufficient in the initial arrangement. With a local basis, we include up to octupole order throughout the optimizations.

The optimization results are presented in Fig. 1. Spheres with a relative permittivity of 6.25 in vacuum are initially arranged along a circle with a radius of 400 nm [see the arrangement depicted with red spheres in Fig. 1 (b)]. In the chosen example, we have opted to consider six spheres with a radius of 80 nm. Similar results were obtained with a larger or smaller number of spheres with different radii as initial conditions. However, if the number is too large, it overly constrains the optimization search space, and the performance degrades. The initial arrangement should be set on a larger circle to provide sufficient design freedom. To set a baseline, we initially computed the F/B scattering ratio of this given structure upon

illumination with a y -polarized plane wave propagating in the z -direction in the wavelength range from 400 to 1,000 nm. The F/B scattering ratio of this initial configuration is shown in Fig. 1 (c). A clear peak of 10 is observed at around 450 nm.

Optimization of the F/B scattering ratio is performed at the design wavelength of 800 nm. The positions and radii of the spheres are adjusted in each iteration, respecting the overlap constraints. We initialize the spheres with small radii to avoid early overlap constraint violations during optimization. As can be seen in Fig. 1 (c), the final F/B ratio reaches 80 at the design wavelength. Figure 1 (a) shows that the algorithm has converged after 40 iterations, where the achievable F/B scattering ratio reaches a plateau. We may also observe a significant broadband increase of the total scattering cross section, as demonstrated in Fig. 1 (d).

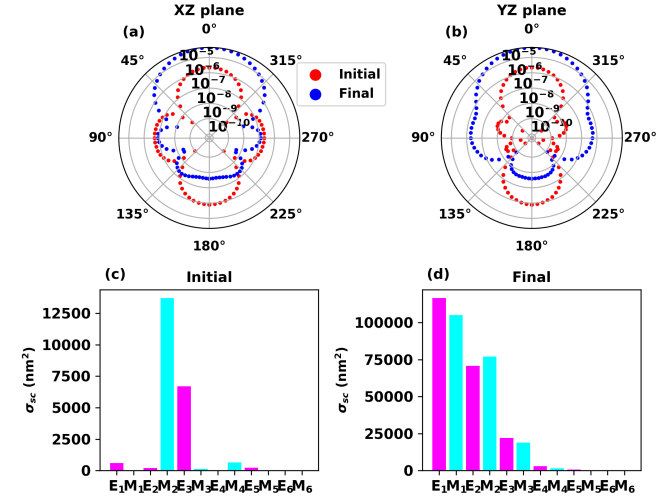


FIG. 2: Top: Polar plots of the radiation pattern in the XZ (a) and YZ planes (b). Bottom: Multipole contributions to the scattered cross-section of the initial (c) and final arrangement (d). For visual clarity, bars representing electric multipole contributions are shown in magenta, while magnetic multipoles are in cyan. All results are shown at the design wavelength.

The optimized structure exhibits a pattern obtained in alternative optimizations with other initial arrangements as well, with some spheres shifted along the z -direction. Generally, it is observed that the spheres move closer to each other and increase in size. The initial arrangement is 6-fold symmetrical. However, the illumination breaks the symmetry for the gradients except for the mirror symmetry. For this reason, the final arrangement also possesses this symmetry. However, since the target scattering pattern is not symmetric about z -axis, the optimized structure necessarily breaks the initial 6-fold rotational symmetry by introducing unequal displacements along z . The total scattering is also increased, which is expected given the larger sizes of the spheres obtained in the final arrangement.

To illustrate the changes, the radiation pattern and multipole decomposition for the initial and final arrangements at the design wavelength are shown in Fig. 2. The radiation pat-

tern, plotted here in log scale in Fig. 2 (a) and (b), exhibits differences between the two considered planes, particularly in the strength of the sidelobes. Both radiation patterns indicate that the higher final ratio was achieved through a reduction in backward scattering and an increase in forward scattering at the same time.

The multipole decomposition of the scattering response at the design wavelength as shown in Fig. 2 (c) and (d) was performed by expanding the final T-matrix about a single origin, necessitating the inclusion of higher-order multipoles, i.e., this is the response expressed in the global T-matrix. In the initial arrangement, total scattering is low and dominated by two multipolar components: magnetic quadrupole (61%) and electric octupole (30%) (Fig. 2 (c)). The increased scattering strength in the optimized structure is achieved by enhancing the contribution of individual multipoles—gradually, decreasing in strength for higher orders, and effectively balancing the electric and magnetic components of the same order (dipoles: 28% and 25.2%, quadrupoles: 17% and 18.5%, octupoles: 5.3% and 4.5%), as shown in Fig. 2 (d). The pattern is consistent with the common understanding of the Kerker effect. Specifically, the different electric and magnetic multipoles contribute comparably to the total scattering response. Thanks to the suitable interference, the scattered light directly in the forward direction is two orders of magnitude larger than the light directly scattered in the backward direction. We note that, in the general case, it is not required to have equal contributions from electric and magnetic multipoles^{62,63}.

Finally, we verify the functionality of the designed structures in dedicated experiments. To perform the experiments, we chose microwave frequencies. This range is experimentally less demanding, while the same arrangement can, in principle, be implemented at optical frequencies, provided suitable material and nanofabrication method are used. To prepare the experiments, the optimization was repeated using the experimentally measured material parameters of ABS plastic, which was chosen as the material from which the spheres were made. The target wavelength was 10 cm, corresponding to a target frequency of 3 GHz. The same initial cluster arrangement was used as the starting point for the optimization, and the result of the optimization was very similar to the design introduced above. Both the initial and optimized arrangements were fabricated using 3D-printing and encapsulated in foam. The foam has electromagnetic properties close to air at the operating band and serves as a mechanical scaffold that maintains the spheres at their designed positions. With that, we can assure that the spheres are arranged as designed and structurally stable.

The electromagnetic scattering responses of the clusters were measured in the direct forward and backward directions, with the results shown in Fig. 3c. The simulation results with CST Studio Suite are demonstrated as a cross-check in Fig. 3d. Generally, an excellent agreement can be seen, and we observe a tremendously enhanced forward-to-backward scattering ratio of 10^2 and beyond at or close to the design frequency. Slight deviations occur, nevertheless, between experiment and simulations. After testing the sensitivity of the response to uncertainties in some selected parameters, we at-

tribute the frequency shift of the observed response peak to minor uncertainties in the positions of the spheres, rather than to inconsistencies in the material properties. The weakening of a secondary resonance with an enhanced forward-to-backward scattering ratio at higher frequencies, as seen in the experiment when compared to the simulations, can be related to the observation that, in the integrated quantity, this peak is even less pronounced. Thus, the experimental conditions in the measurement process effectively approach this situation as well. Experimentally, we are not measuring the scattering into a single direction, as considered in the simulation, but a small but finite angular domain. That weakens the observed secondary resonance. Further details of the experimental realization, along with more measurement results, are provided in the Supplementary Information. Nevertheless, we can conclude from these experiments that the inverse designs we provide can be translated into tangible technology.

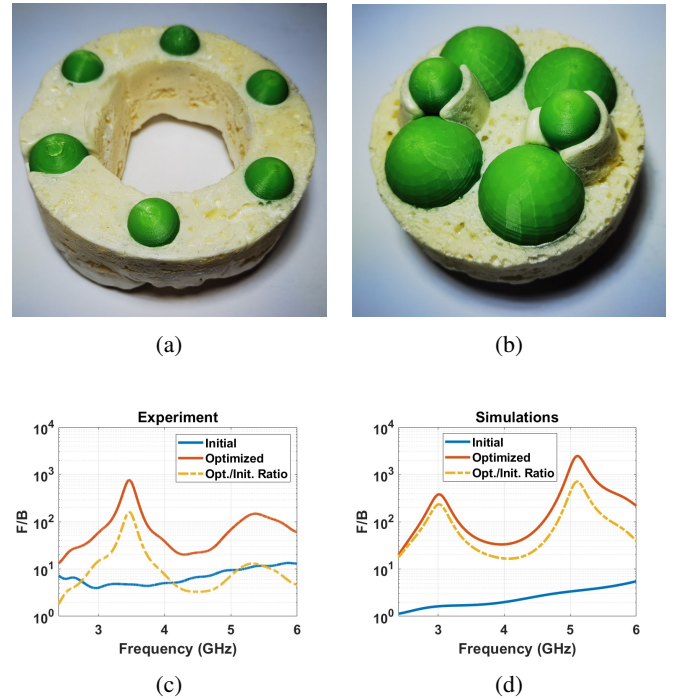


FIG. 3: Fabricated samples using 3D-printing and foam hosting: (a) the initial cluster and (b) optimized cluster. The ratio of directly forward (0°) to directly backward (180°) scattering under y -polarized plane wave for both structures – initial (solid blue) and optimized (solid red), and their quotient (optimized/initial, dash-dotted): (c) experimental measurements and (d) CST numerical simulations.

B. Metasurfaces with complex unit cell

Next, we discuss as a second example the inverse design of a metasurface that consists of a periodic arrangement of a complex unit cell. Each unit cell contains five spheres. Our purpose is to achieve a strongly polarization-dependent reflec-

tion. As discussed in⁷⁵, the optical response of individual scatterers is modified by the lattice interaction, and the overlap of multipole contributions with different parity can cancel light propagation in one direction. Now, if the unit cell breaks 4-fold symmetry, it is possible to achieve this cancellation effect for only one of the polarizations of the incident plane wave.

The objective function is defined as:

$$\text{FOM} = |R_y - R_x|, \quad (9)$$

where R denotes the total reflectance, and the subscript indicates the x - or y -polarization of the incident light.

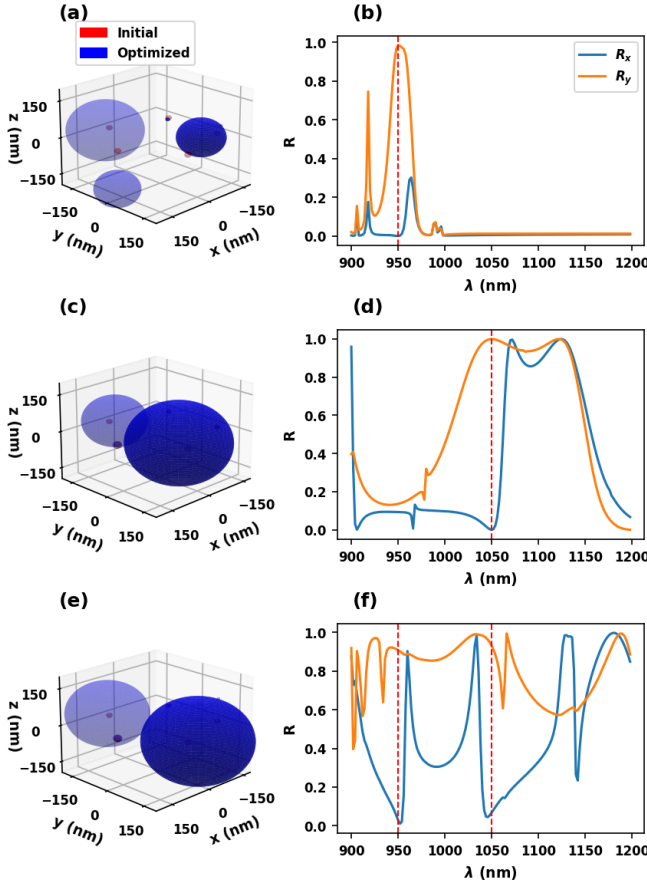


FIG. 4: Initial (red) and optimized (blue) constituents of the metasurface unit cell targeting reflection peak for one linear polarization of the incident light and a low reflection for the other one at (a) 950 nm, (b) 1050 nm, and (c) simultaneously

950 nm and 1050 nm. The transparency of each sphere decreases with its proximity to the viewer. Panels (d–f) show corresponding reflection spectra for x -polarized (blue curves) and y -polarized (orange curves) incident light. Vertical red dashed lines indicate the target wavelength(s).

Clearly, when setting the initial arrangement, the symmetries can be broken or preserved. We choose an odd number of spheres, five in total, and position them in a circle such that one sphere lies on the x -axis. This way, the unit cell is symmetric with respect to the x -axis, but not to the y -axis. Hence,

we can expect the cancellation to occur for the x -polarized incident field.

The setup parameters include the initial radius of a single sphere and the radius of the circle along which the spheres are arranged. The example considers silicon spheres with relative permittivity values taken from⁷⁶ embedded in a medium with a relative permittivity of 2.25. Each sphere of the initial arrangement has a radius of 10 nm, the radius of the circle is set to 170 nm, and the pitch is 600 nm. The small size of the initial spheres is chosen to ensure ample free space for the scatterers to move and grow during the optimization process. The design wavelengths selected below exceed the unit cell size, ensuring operation within the non-diffractive regime. The incident field is always a plane wave propagating along the z -axis (normal incidence), and it is either x - or y -polarized.

To tune the resonance, we leave the radii and positions of the independent scatterers in the unit cell as free parameters while keeping the lattice constant fixed in the optimization. The spheres are not allowed to overlap and shrink below 5 nm, as in the previous example. The no-overlap condition was modified to enforce an additional minimal separation 5 nm between spheres, based on the observation that they tend to approach each other at subnanometer distances. An additional constraint restricts the position of the spheres within the circumscribing sphere of the unit cell, since the T-matrix of the arrangement in the unit cell is expanded about a common origin. Multipole contributions up to 8th order are included during optimization, and the final arrangements are recalculated up to 15th order. All optimizations run for 200 iterations and reach convergence within this number of steps.

From optimization at different wavelengths, we note that the optimizer can reach the high reflectance value for many wavelengths within a particular wavelength range, and we demonstrate the optimization results obtained at 950 and 1050 nm in Fig. 4(a-b) and (d-f).

To explore a more challenging design, we also focus on achieving dual-band performance. It is realized by applying an adaptive weighting scheme to balance the optical response at two wavelengths. The objective is defined as follows:

$$f_i = |R_y(\lambda_i) - R_x(\lambda_i)|, \quad i = 1, 2 \quad (10)$$

$$\text{FOM} = \frac{2f_1f_2 + \epsilon \min(f_1, f_2)}{f_1 + f_2 + \epsilon}, \quad (11)$$

where ϵ is a small regularization parameter. The regularization ensures that the term with the smaller value is given greater emphasis. It can be observed in Fig. 4 (f), that for the incident plane wave with x -polarization sharp peaks are produced, while a plane wave with y -polarization is responsible for the wide resonance curve in reflectance.

For all of the optimizations, we observe that the number of spheres is effectively reduced, as the significant response is only obtained from two to three spheres that have increased in size considerably. This is to be expected given the limited space available during optimization. Optimizations that omit the shrunken spheres from the initial configuration reproduce the same final arrangement.

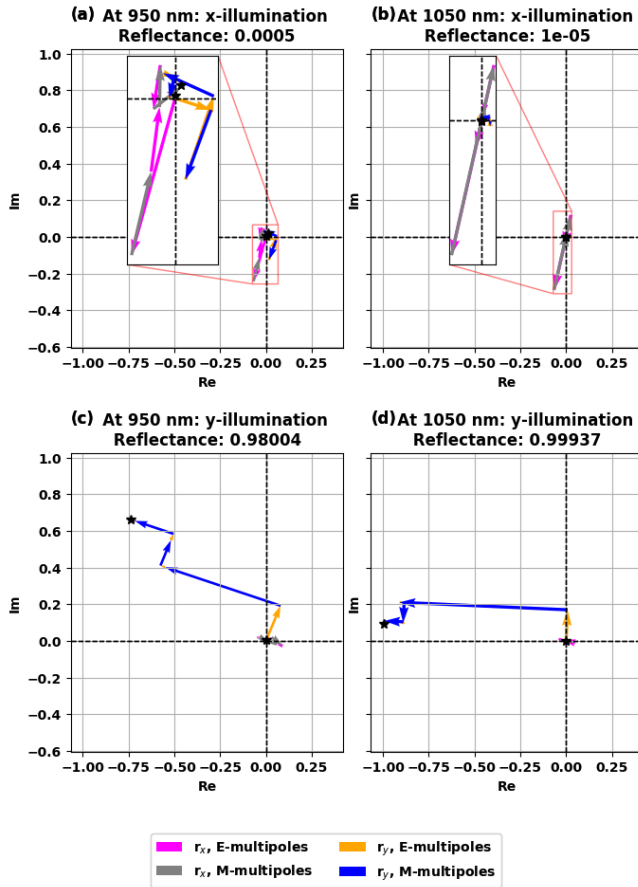


FIG. 5: Phasor diagram of contributions of electric and magnetic multipoles to the backward-scattered field

coefficients. Panels (a, c) show the results for a non-diffractive metasurface optimized at 950 nm, while panels (b, d) demonstrate the results of optimization at 1050 nm. Starting from 0, the vectors build up as E_1, M_1, E_2, M_2 , and so on, where E stands for electric and M for magnetic multipoles, which is followed by the multipole order. Each panel shows the phasor build-up of x - and y -polarized scattered field components separately. However, the cross-polarized components are negligible. For both optimized structures illuminated with x -polarized light, in a) and c), the electric and magnetic multipole contributions cancel each other, whereas in b) and d), under y -illumination, they sum up to a high value of reflectance.

To investigate the underlying behavior of the T-matrix, the phasor diagrams of the contributions of different multipoles to the components of the complex reflection coefficient are shown in Fig. 5 for the single wavelength optimized geometries, and in Fig. 6 for the dual-wavelength optimized geometry. We work with T-matrices that already include lattice interactions. As the coefficients contributing to the backward-propagating field are needed, we switch to plane wave basis quantities for clarity.

In Appendix B, exact formulas are provided to compute the expansion coefficient in a plane wave basis knowing the

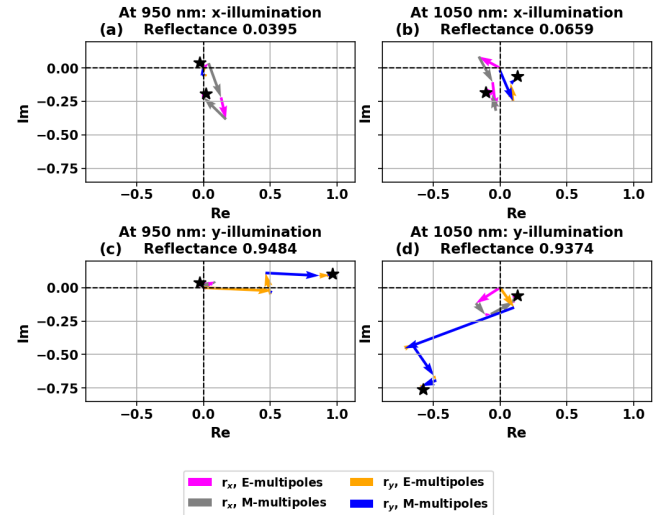


FIG. 6: Phasor diagram of contributions of electric and magnetic multipoles to the complex reflection coefficient. The non-diffractive metasurface was optimized for maximum reflectance contrast at simultaneously 950 nm and 1050 nm. Panels a) and b) demonstrate the contributions of multipoles to the complex reflection coefficient for x - and y -components of the scattered field, when the metasurface is illuminated by x -polarized plane wave, which results in minimal final reflectance. In panels c) and d), the incident plane wave is y -polarized, and the final reflectance is high. Each panel shows the phasor build-up of x - and y -polarized scattered field components separately.

expansion coefficients in the spherical wave basis, which involve a summation procedure over all orders l and m . Rather than performing the entire summation at once, we separate the sum over particular multipole orders and polarizations, and derive the corresponding partial S-matrices, each accounting only for electric dipole, magnetic dipole, and so on. Next, the complex-valued reflection coefficients are calculated by multiplying the S_{\downarrow} block with the vector representing the expansion coefficients of the plane wave, which contains one and zero according to the polarization. The final reflectance is:

$$R = \left| \sum_{i=1}^N r_i \right|^2, \quad (12)$$

where $N = 2l_{\max}$. The reflection coefficients corresponding to each multipole with a definite total angular momentum and parity are depicted as phasors, and their vector sum is the total reflection coefficient. Although the expansion includes 15 multipole orders, the phasor diagram shows that only up to octupole order contributions are significant.

In Fig. 5, the electric and magnetic multipoles cancel each other almost perfectly under x -polarized light. For y -illumination, the contributions add up to nearly perfect reflectance. The cross-polarized terms are negligible. Meanwhile, for dual-wavelength optimization in Fig. 6, the situation is not the same. We observe a few strong multipole contributions under y -polarized illumination that are not compen-

sated, as expected. For the x -polarized incident field, there are components of smaller magnitude, with some of the phasors directed in opposite directions. However, there is no explicit pairwise cancellation characteristic of the Kerker effect. In both illumination scenarios, the cross-polarized field components are non-zero and of similar magnitude, indicating that this can be disregarded when finding an actual reason behind the difference in outcomes. Clearly, the dual-band objective is more complicated to fulfill, and one could not achieve total cancellation; however, the optimization procedure was able to find a close enough solution, and the reflectance for x -polarized light can be considered negligible.

The demonstrated results reinforce the conclusion that gradient-based methods are a powerful tool for optimization. As for all local optimization techniques, the achievable results can be sensitive to the choice of initial conditions. Common approaches to avoid convergence to suboptimal local maxima include combining these techniques with global optimization methods or performing multiple runs with varied initial conditions. Nevertheless, the gradient-based framework is essential for fine-tuning design parameters.

IV. CONCLUSION

We have developed and evaluated a differentiable computational framework for the inverse design of nanophotonic systems based on the T-matrix method. The Python code is open access (<https://github.com/tfp-photonics/dreams>). We applied this to design various structures consisting of elaborate arrangements of spherical scatterers in finite clusters and on periodic lattices. A key strength of our framework is its ability to simultaneously optimize the positions and radii of spheres, leveraging strong multipolar interactions. This capability extends directly to the positions of arbitrarily shaped scatterers, and the method can be used together with other differentiable solvers to compute derivatives with respect to any geometrical parameter. The required derivatives are efficiently obtained through automatic differentiation. Even a moderate number of parameters generates an ample design space, making brute-force parameter sweeps and some global optimization techniques infeasible.

Specifically, we demonstrate a maximized forward-to-backward scattering ratio for a cluster of spheres and a tailored polarization-dependent reflectance for a metasurface with a complex unit cell. Both case studies involve the cancellation of scattered fields in a specific direction, exemplifying the generalized Kerker effect. The comprehensive T-matrix approach easily reveals the contribution of different multipoles to the optimized scattered field. We ensure that the simulation method itself does not impose restrictions on the inclusion of higher-order multipolar components in the optical response. From the optimization curves, we observe that the optimizations start from comparatively low initial values and converge to high-performance solutions that respect all constraints. Combining multiple objectives, as seen in the example of dual-wavelength optimization, achieves the desired functionality, even if it does not strictly follow the expected

underlying mechanism. This further enhances the flexibility of the design framework.

This work opens new possibilities for the automated, high-fidelity design of complex nanophotonic architectures where multipolar interference plays a central role. By integrating differentiable programming with the T-matrix formalism, it lays the groundwork for scalable, mechanism-agnostic optimization across diverse application domains, from directional scattering to metasurface engineering. The framework is well-positioned to accelerate the inverse design of functional photonic systems beyond traditional heuristic-guided approaches.

Finally, we wish to add that at the time of the submission, we became aware of a manuscript developing similar ideas⁷⁷. This underpins the timeliness and importance of the differentiable formulation of algorithms that solve multiple-scattering problems, a key requirement for inverse design of photonic nanostructures.

ACKNOWLEDGMENTS

N.A. and C.R. acknowledge financial support by the Federal Ministry of Research, Technology and Space (BMFTR) within the project DAPHONA (16DKWN039). J.D.F. and C.R. acknowledge financial support by the Helmholtz Association in the framework of the innovation platform “Solar TAP”. C.R. acknowledges support from the German Research Foundation within the Excellence Cluster 3D Matter Made to Order (EXC 2082/1 under project number 390761711) and by the Carl Zeiss Foundation. N.A. and J.D.F. acknowledge support from the Karlsruhe School of Optics and Photonics (KSOP). The work of D.V. was supported by the 1.1.1.9 Activity “Post-doctoral Research” Research application No 1.1.1.9/LZP/1/24/166 “Linear Industrial Monitoring System based on Hyperspectral Cameras and AI Algorithms (LIF-HYCAI)”. TAU Team acknowledges Israel Science Foundation (ISF Grant Number 1115/23).

DATA AVAILABILITY STATEMENT

The data that support the findings of this study are openly available at⁶⁰.

¹M. M. Elsawy, S. Lanteri, R. Duvigneau, J. A. Fan, and P. Genevet, *Laser & Photonics Reviews* **14**, 1900445 (2020).

²S. D. Campbell, D. Sell, R. P. Jenkins, E. B. Whiting, J. A. Fan, and D. H. Werner, *Optical Materials Express* **9**, 1842 (2019).

³K. Yao, R. Unni, and Y. Zheng, *Nanophotonics* **8**, 339 (2019).

⁴Q. Wang, M. Makarenko, A. Burguete Lopez, F. Getman, and A. Fratalochi, *Nanophotonics* **11**, 2483 (2022).

⁵P. Bennet, D. Langevin, C. Essoual, A. Khaireh-Walieh, O. Teytaud, P. Wiecha, and A. Moreau, *Journal of the Optical Society of America B* **41**, A126 (2024).

⁶P. R. Wiecha, A. Arbouet, C. Girard, and O. L. Muskens, *Photonics Research* **9**, B182 (2021).

⁷T. Ma, M. Tobah, H. Wang, and L. J. Guo, *Opto-Electronic Science* **1**, 210012 (2022).

⁸D. Sell, J. Yang, S. Doshay, R. Yang, and J. A. Fan, *Nano letters* **17**, 3752 (2017).

⁹Z. Lin, V. Liu, R. Pestourie, and S. G. Johnson, *Optics express* **27**, 15765 (2019).

¹⁰A. Mirzaei, A. E. Miroshnichenko, I. V. Shadrivov, and Y. S. Kivshar, *Scientific reports* **5**, 9574 (2015).

¹¹Z. Li, L. Stan, D. A. Czaplewski, X. Yang, and J. Gao, *Optics Letters* **44**, 114 (2018).

¹²P. R. Wiecha, C. Majorel, C. Girard, A. Cuche, V. Paillard, O. L. Muskens, and A. Arbouet, *Optics express* **27**, 29069 (2019).

¹³P.-I. Schneider, X. G. Santiago, C. Rockstuhl, and S. Burger, in *Digital Optical Technologies 2017*, Vol. 10335 (SPIE, 2017) pp. 141–149.

¹⁴P. R. Wray, E. G. Paul, and H. A. Atwater, *Nanophotonics* **13**, 183 (2024).

¹⁵K. Eggensperger, M. Feurer, F. Hutter, J. Bergstra, J. Snoek, H. Hoos, K. Leyton-Brown, *et al.*, in *NIPS workshop on Bayesian Optimization in Theory and Practice*, Vol. 10 (2013) pp. 1–5.

¹⁶G. Angeris, J. Vučković, and S. Boyd, *Optics Express* **29**, 2827 (2021).

¹⁷X. Shen, Z. Wu, and Y. Liu, *IEEE Transactions on Antennas and Propagation* **71**, 3100 (2023).

¹⁸J. Jiang, M. Chen, and J. A. Fan, *Nature Reviews Materials* **6**, 679 (2021).

¹⁹Z. Li, R. Pestourie, Z. Lin, S. G. Johnson, and F. Capasso, *ACS Photonics* **9**, 2178 (2022).

²⁰M. P. Bendsoe and O. Sigmund, *Topology optimization: theory, methods, and applications* (Springer Science & Business Media, 2013).

²¹A. Y. Piggott, J. Petykiewicz, L. Su, and J. Vučković, *Scientific reports* **7**, 1786 (2017).

²²Y. Augenstein and C. Rockstuhl, *ACS photonics* **7**, 2190 (2020).

²³A. M. Hammond, A. Oskooi, S. G. Johnson, and S. E. Ralph, *Optics Express* **29**, 23916 (2021).

²⁴A. Luce, R. Alae, F. Knorr, and F. Marquardt, *Machine Learning: Science and Technology* (2023).

²⁵T. W. Hughes, I. A. Williamson, M. Minkov, and S. Fan, *ACS Photonics* **6**, 3010 (2019).

²⁶S. Hooten, P. Sun, L. Gantz, M. Fiorentino, R. Beausoleil, and T. Van Vaerenbergh, *Laser & Photonics Reviews* **19**, 2301199 (2025).

²⁷B. Vial and Y. Hao, *Mathematics* **10**, 3912 (2022).

²⁸T. Xue, S. Liao, Z. Gan, C. Park, X. Xie, W. K. Liu, and J. Cao, *Computer Physics Communications* **291**, 108802 (2023).

²⁹V. Liu and S. Fan, *Computer Physics Communications* **183**, 2233 (2012).

³⁰J. P. Hugonin and P. Lalanne, *arXiv preprint arXiv:2101.00901* (2021).

³¹S. Colburn and A. Majumdar, *Communications Physics* **4**, 65 (2021).

³²Z. Zhu and C. Zheng, *Optics Express* **28**, 37773 (2020).

³³S. So, J. Kim, T. Badloe, C. Lee, Y. Yang, H. Kang, and J. Rho, *Advanced Materials*, 2208520 (2023).

³⁴C. Kim and B. Lee, *Computer Physics Communications* **282**, 108552 (2023).

³⁵W. Jin, W. Li, M. Orenstein, and S. Fan, *ACS Photonics* **7**, 2350 (2020).

³⁶A. S. Backer, *Optics express* **27**, 30308 (2019).

³⁷T. Phan, D. Sell, E. W. Wang, S. Doshay, K. Edee, J. Yang, and J. A. Fan, *Light: Science & Applications* **8**, 48 (2019).

³⁸S. Ponomareva, A. Patoux, C. Majorel, A. Azéma, A. Cuche, C. Girard, A. Arbouet, and P. Wiecha, *SciPost Physics Codebases*, 060 (2025).

³⁹V. Yannopapas and A. G. Vanakaras, *Physical Review B—Condensed Matter and Materials Physics* **84**, 085119 (2011).

⁴⁰D. Pal and A. F. Koenderink, *Laser & Photonics Reviews* **19**, e02199 (2025).

⁴¹K. Tanaka, D. Arslan, S. Fasold, M. Steinert, J. Sautter, M. Falkner, T. Pertsch, M. Decker, and I. Staude, *ACS nano* **14**, 15926 (2020).

⁴²G. Salerno, R. Heilmann, K. Arjas, K. Aronen, J.-P. Martikainen, and P. Törmä, *Physical Review Letters* **129**, 173901 (2022).

⁴³D. Beutel, I. Fernandez-Corbaton, and C. Rockstuhl, *Computer Physics Communications* **297**, 109076 (2024).

⁴⁴A. Zhan, T. K. Fryett, S. Colburn, and A. Majumdar, *Applied optics* **57**, 1437 (2018).

⁴⁵A. Zhan, R. Gibson, J. Whitehead, E. Smithf, J. R. Hendrickson, and A. Majumdar, *Science advances* **5**, eaax4769 (2019).

⁴⁶V. Igoshin, A. Kokhanovskiy, and M. Petrov, *Optics Letters* **50**, 1735 (2025).

⁴⁷M. Tsukerman, K. Grotov, and P. Ginzburg, *arXiv preprint arXiv:2511.05357* (2025).

⁴⁸J. D. Fischbach, F. Betz, N. Asadova, P. Tassan, D. Urbonas, T. Stöferle, R. F. Mahrt, S. Burger, C. Rockstuhl, F. Binkowski, *et al.*, *Advanced Theory and Simulations* **8**, 2400989 (2025).

⁴⁹J. D. Jackson, “Classical electrodynamics,” (1998).

⁵⁰O. R. Cruzan, *Quarterly of Applied Mathematics* **20**, 33 (1962).

⁵¹R. N. Suryadharma, M. Fruhnert, I. Fernandez-Corbaton, and C. Rockstuhl, *Physical Review B* **96**, 045406 (2017).

⁵²P. P. Ewald, *Annalen der physik* **369**, 253 (1921).

⁵³D. Beutel, I. Fernandez-Corbaton, and C. Rockstuhl, *Physical Review A* **107**, 013508 (2023).

⁵⁴A. G. Baydin, B. A. Pearlmutter, A. A. Radul, and J. M. Siskind, *Journal of machine learning research* **18**, 1 (2018).

⁵⁵J. Hückelheim, H. Menon, W. Moses, B. Christianson, P. Hovland, and L. Hascoët, *Wiley Interdisciplinary Reviews: Data Mining and Knowledge Discovery* **14**, e1555 (2024).

⁵⁶M. Blondel and V. Roulet, *arXiv preprint arXiv:2403.14606* (2024).

⁵⁷J. Bradbury, R. Frostig, P. Hawkins, M. J. Johnson, C. Leary, D. Maclaurin, G. Necula, A. Paszke, J. VanderPlas, S. Wanderman-Milne, and Q. Zhang, “JAX: composable transformations of Python+NumPy programs,” (2018).

⁵⁸A. Paszke, S. Gross, F. Massa, A. Lerer, J. Bradbury, G. Chanan, T. Killeen, Z. Lin, N. Gimelshein, L. Antiga, *et al.*, *Advances in neural information processing systems* **32** (2019).

⁵⁹M. Abadi, P. Barham, J. Chen, Z. Chen, A. Davis, J. Dean, M. Devin, S. Ghemawat, G. Irving, M. Isard, *et al.*, in *12th USENIX symposium on operating systems design and implementation (OSDI 16)* (2016) pp. 265–283.

⁶⁰“dreams: differentiable multiscattering code,” <https://github.com/tfp-photonics/dreams> (2025).

⁶¹A. Alu and N. Engheta, *Journal of Nanophotonics* **4**, 041590 (2010).

⁶²R. Alae, R. Filter, D. Lehr, F. Lederer, and C. Rockstuhl, *Optics letters* **40**, 2645 (2015).

⁶³W. Liu and Y. S. Kivshar, *Optics express* **26**, 13085 (2018).

⁶⁴A. E. Miroshnichenko, A. B. Evlyukhin, Y. F. Yu, R. M. Bakker, A. Chipouline, A. I. Kuznetsov, B. Luk'yanchuk, B. N. Chichkov, and Y. S. Kivshar, *Nature communications* **6**, 8069 (2015).

⁶⁵H. K. Shamkhi, K. V. Baryshnikova, A. Sayanskiy, P. Kapitanova, P. D. Terekhov, P. Belov, A. Karabchevsky, A. B. Evlyukhin, Y. Kivshar, and A. S. Shalin, *Physical review letters* **122**, 193905 (2019).

⁶⁶Z. Ruan and S. Fan, *Physical review letters* **105**, 013901 (2010).

⁶⁷R. W. Ziolkowski, *Physical Review X* **7**, 031017 (2017).

⁶⁸S. Krasikov, M. Odit, D. Dobrykh, I. Yusupov, A. Mikhailovskaya, D. Shakirova, A. Shcherbakov, A. Slobozhanyuk, P. Ginzburg, D. Filonov, *et al.*, *Physical Review Applied* **15**, 024052 (2021).

⁶⁹T. Lindström and A. Roos, *Review of Scientific Instruments* **71**, 2270 (2000).

⁷⁰D. Payne, M. Charlton, and D. Bagnall, *Applied Optics* **54**, 7224 (2015).

⁷¹M. Kim and W. D. Philpot, *Applied optics* **44**, 6952 (2005).

⁷²J. Jung, T. Søndergaard, T. G. Pedersen, K. Pedersen, A. N. Larsen, and B. B. Nielsen, *Physical Review B—Condensed Matter and Materials Physics* **83**, 085419 (2011).

⁷³H. U. Ulriksen, T. Søndergaard, T. G. Pedersen, and K. Pedersen, *Optics Express* **27**, 14308 (2019).

⁷⁴K. Svanberg, vol **1**, 1 (2007).

⁷⁵V. E. Babicheva and A. B. Evlyukhin, *Laser & Photonics Reviews* **11**, 1700132 (2017).

⁷⁶C. Schinke, P. Christian Peest, J. Schmidt, R. Brendel, K. Bothe, M. R. Vogt, I. Kröger, S. Winter, A. Schirmacher, S. Lim, *et al.*, *Aip Advances* **5** (2015).

⁷⁷O. Jackson, S. De Liberato, O. L. Muskens, and P. R. Wiecha, *arXiv preprint*.

Appendix A: Custom derivative

The derivative of the spherical Bessel (and Hankel) functions is calculated using the recurrence relation. The special case of zero argument has to be treated accordingly. For $v > 1$, it can be set to zero, while for $v = 1$, the Taylor series expansion of the *sinc* gives a non-zero number.

Listing 1: Example: Custom spherical Bessel function in JAX

```

1 def spherical_jn(v, z):
2     z = z.astype(np.result_type(complex, z.
3         dtype))
4
5     return jax.pure_callback(
6         lambda v, z: mod_jn(v, z).astype(z.
7             dtype),
8         jax.ShapeDtypeStruct(
9             shape=np.broadcast_shapes(v.
10                 shape, z.shape),
11                 dtype=z.dtype
12             ),
13             v, z,
14             vmap_method="legacy_vectorized"
15         )
16
17 @spherical_jn.defjvp
18 def _jv_jvp(primals, tangents):
19     """
20     Custom JVP rule for spherical Bessel
21     function.
22     """
23     v, z = primals
24     _, z_dot = tangents # v_dot = 0 since
25     # v is integer.
26
27     jv_v_z = spherical_jn(v, z)
28     jv_plus_1 = spherical_jn(v + 1, z)
29
30     small_z = np.abs(z) < 1e-8
31
32     djv_dz = np.where(
33         (small_z & (v != 1)), 0.0j,
34         np.where(
35             (small_z & (v == 1)), 1/3,
36             v * jv_v_z / z - jv_plus_1
37         )
38     )
39
40     return jv_v_z, z_dot * djv_dz

```

coefficients are given by:

$$\begin{pmatrix} C_{\text{TE}}(g) \\ C_{\text{TM}}(g) \end{pmatrix} = \sum_{\ell=1}^{\ell_{\max}} \sum_{m=-\ell}^{\ell} F_{\ell m}(g) \underbrace{\begin{pmatrix} \tau_{\ell m}(\theta_g) & \pi_{\ell m}(\theta_g) \\ \pi_{\ell m}(\theta_g) & \tau_{\ell m}(\theta_g) \end{pmatrix}}_{A_{\ell m}(\theta_g)} \begin{pmatrix} p_{e,\ell m} \\ p_{m,\ell m} \end{pmatrix}, \quad (\text{B2})$$

where $\pi_{\ell m}(\theta_g)$ and $\tau_{\ell m}(\theta_g)$ are the two angle-dependent functions defined in terms of the associated Legendre functions P_l^m :

$$\pi_{\ell m}(\theta) = \frac{m}{\sin \theta} P_l^m(\cos \theta), \quad \tau_{\ell m}(\theta) = \frac{d}{d\theta} P_l^m(\cos \theta). \quad (\text{B3})$$

Finally,

$$F_{\ell m}(g) = - \frac{i\pi N_{\ell m}}{a k i^{\ell-m}} \frac{1}{\sqrt{1 - |\mathbf{k}_{\parallel}|^2 + g^2/k^2}}, \quad (\text{B4})$$

$$\cos \theta_g = \frac{\sqrt{k^2 - |\mathbf{k}_{\parallel}|^2}}{k}.$$

where $N_{\ell m}$ is the normalization constant of the VSW, and a is the area of the unit cell.

Appendix B: Translation from periodic vector spherical wave coefficients to plane wave coefficients

The scattered field summed over the periodic lattice in the plane wave basis can be written as follows:

$$\mathbf{E}_{\text{scat}}^{(\text{lattice}),d}(\mathbf{r}) = \sum_{g \in \Lambda^*} e^{i(\mathbf{k}_{\parallel} + g) \cdot \mathbf{r}} \left[C_{\text{TE}}(g) \hat{e}_{\text{TE}}(\mathbf{k}_{\parallel} + g, d) + C_{\text{TM}}(g) \hat{e}_{\text{TM}}(\mathbf{k}_{\parallel} + g, d) \right]. \quad (\text{B1})$$

In the expression above, \mathbf{k}_{\parallel} is the tangential component of the plane wave, and g is the diffraction order. The expansion

SUPPLEMENTARY INFORMATION: EXPERIMENTAL REALIZATION AT MICROWAVE FREQUENCIES

In this supplement, we describe efforts that demonstrate the functionality of the designed devices at microwave frequencies. This required us to perform initial simulations adjusted to the experimental constraints that are described first. Then, we outline details on how the samples were fabricated, and finally, we explain the details of the characterization. A summary of these results had been included in the main document.

S1.1. Simulation

Although the initial designs in the main part of the manuscript were described at optical frequencies, we have implemented, verified, and scaled an experimental setup that allows for observation at microwave frequencies. Thanks to the scale invariance of Maxwell's equations, this is generally a valid approach, as long as the material properties are identical. Since the material properties are different than those considered in the main text, we resimulated the electromagnetic response from the samples with the experimentally accessible material properties, and we describe these simulations in this subsection at first.

First, the frequency around 3 GHz was taken as the design frequency, corresponding to a wavelength of 10 cm. That is in agreement with the experimental equipment available to us. The spheres were made from Acrylonitrile butadiene styrene (ABS), a common thermoplastic polymer. As retrieved from dedicated measurements described in the experimental subsection further below, the material was characterized by a permittivity of $\epsilon = \epsilon' + i\epsilon'' = 2.54 + i0.26$. The approach to optimize the spheres' position and radius, as described in the main text, was applied again using this adjusted permittivity value. The main purpose of the design has been to optimize the forward-to-backward scattering ratio. Identical to the scenario considered in the main text, the cluster consisted of six spheres. The incident wave is y -polarized as in the main text. The resulting positions and radii, normalized by wavelength, are shown in the tables below. For comparison, the table also displays the geometrical details of the initial cluster used for reference purposes. All geometrical parameters are normalized to a wavelength of 10 cm.

As the integrated quantity employed during optimization was not measurable with our experimental setup, the subsequent analysis is restricted to scattering at 0° and 180° (forward and backward, respectively).

The initial and optimized configurations, as shown in Figs. S2a-b, were also simulated in CST Microwave Studio. The change in the computational suite was done because it has capabilities aligned with our needs to compare the experimental results to numerical predictions. In the simulations, the structures are illuminated by a linearly polarized plane wave propagating along the z -axis. Both x - and y -polarization are considered separately. Two far-field radar cross-section (RCS) EM probes (for the forward and backward scattering)

TABLE S2: Positions and radii of the spheres that make up the clusters. The details of the initial cluster are presented, along with those of the optimized cluster. Normalization is done with respect to the design wavelength of 10 cm.

(a) Initial cluster					
Sphere	x	y	z	r	
#1	0.50	0.000	0.00	0.10	
#2	0.25	0.433	0.00	0.10	
#3	-0.25	0.433	0.00	0.10	
#4	-0.50	0.000	0.00	0.10	
#5	-0.25	-0.433	0.00	0.10	
#6	0.25	-0.433	0.00	0.10	

(b) Optimized cluster					
Sphere	x'	y'	z'	r'	
#1	0.305	-0.000	0.110	0.130	
#2	0.232	0.281	-0.109	0.218	
#3	-0.234	0.296	-0.105	0.218	
#4	-0.308	0.000	0.113	0.130	
#5	-0.237	-0.280	0.107	0.219	
#6	0.237	-0.280	-0.107	0.219	

from the CST tool library were used to assess the directional scattering. The simulations were performed for the frequency range 2 GHz to 12 GHz (the range corresponds to the capabilities of the laboratory equipment, and includes 3 GHz – the design frequency). The RCS in $\text{dB}(\text{m}^2)$ dispersions are shown in Figs. S2c-f for the initial and optimized clusters. Please focus on the design frequency of 3 GHz. As can be seen, the backward scattering is significantly lower than the forward scattering for both structures, while the optimized structure demonstrates an improvement of 10-40 $\text{dB}(\text{m}^2)$ in forward scattering.

Figure S3 demonstrates the forward-to-backward ratios for each structure (initial – solid blue and optimized – solid red) and their ratio to estimate the advantage of the optimized structure (dash-dotted plot). For the case of x -polarization, an improvement of 1486 times is obtained at 3.39 GHz (Fig. S3a, c), while for the y -polarization it is 233 times at 3 GHz (Fig. S3b, d). This result is achieved because of the appearance of a significant maximum in the forward-to-backward ratio for the optimized structure around the design frequency.

S1.2. Experiments

Samples fabrication

The experimental samples were designed in CST Microwave Studio in accordance with the sizes scaled to the microwaves and exported in STL format for the following 3D-printing with (BCN3D Sigma 3D Printer). ABS was used as the material of the spheres.

The electromagnetic properties of ABS were tested using the open-end coaxial probe method. The method allows us to estimate the complex permittivity. Measurements were made using the Agilent 85070E dielectric probe kit and an E8361C 10 MHz–67 GHz PNA Network Analyzer. Measuring the complex permittivity is crucial for accurately reproducing ex-

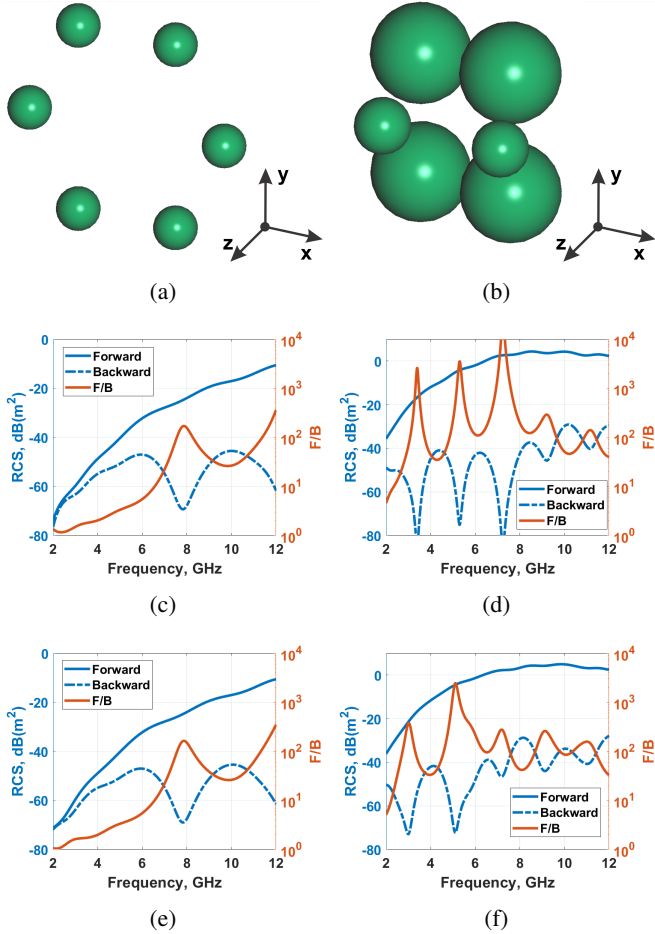


FIG. S2: CST Microwave Studio models of (a) the initial and (b) the optimized cluster, plane wave propagation is along z-axis. (c)-(d) RCS spectra into the forward and backward direction and the forward-to-backward (F/B) ratio for an x-polarization of the illuminating plane wave. (e)-(f) Same plots, but for a y-polarization of the illuminating plane wave.

Please be reminded that the sample was optimized for an operation at 3 GHz.

perimentally measured quantities in simulations. Precise positioning of spatially separated spherical scatterers and their vertical arrangement parallel to the plane of a vertically polarized incident plane wave was achieved by utilizing a special plastic matrix. This matrix held the spheres in place before encapsulation (or casting) with a foam material (Fig. S4).

A complementary model of the initial scatterer group matrix was developed in CST, which assumed the placement of the spheres in “niches” or pockets, ensuring a precise fixed distance between them. After 3D printing of the original spheres from ABS plastic and the matrix model from PLA plastic (any other 3D printing filament with sufficient rigidity is also suitable for the matrix), all spheres were inserted into the matrix at their respective positions. The matrix was then filled with a foam material composed of the following components: Methylene diphenyl diisocyanate, Polyether polyol,

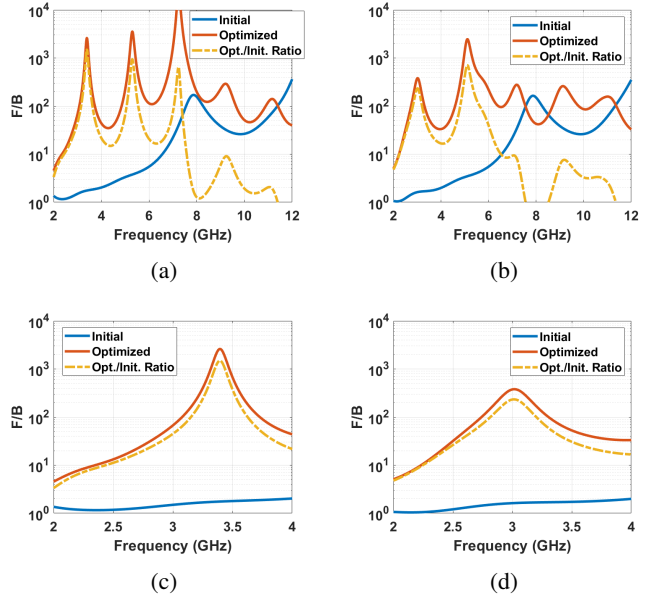


FIG. S3: Simulated forward-to-backward spectra for the models of both structures (initial — solid blue, optimized — solid red) and forward-to-backward dispersion advantage of the optimized structure (dash-dotted) for an illumination with a plane wave propagating in z-direction and a polarization in (a) in x- and in (b) in y-direction, respectively. Zoomed-in plots around the frequency considered in the optimization are shown in (c) and (d), respectively.



FIG. S4: (a) A matrix for spherical electromagnetic scatterers made of black PLA plastic; and (b) an example of the spheres’ arrangement within the system before foam encapsulation.

and 1,1-Dichloro-1-fluoroethane (HCFC-141b). The dielectric parameters of the resulting foam are very close to those of air, as the solidified foam is predominantly composed of air (due to its porous structure).

After filling the spherical scatterer matrix with the foam and its subsequent curing for 24 hours, the original matrix was removed from the scatterers, which became solidified and precisely fixed within the foam. As a result of fabrication, the initial and optimized structures were prepared as shown in Figs. S5a-b.

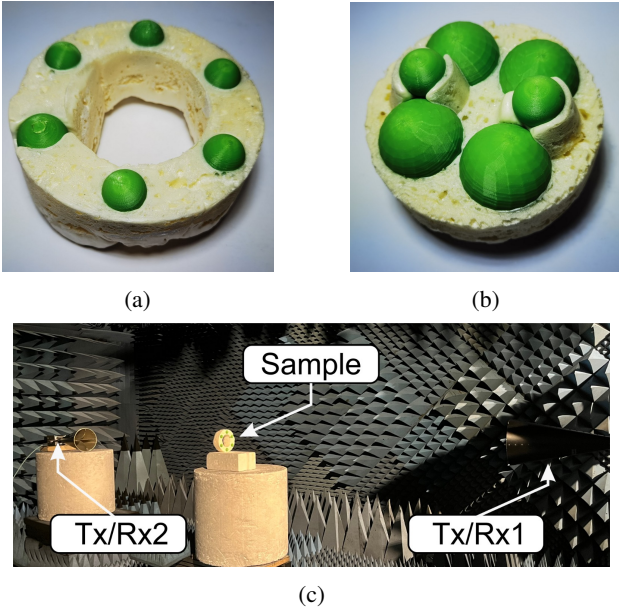


FIG. S5: Fabricated samples using 3D-printing and foam hosting: (a) the initial cluster and (b) optimized cluster. (c) The experimental setup in the anechoic chamber with two horn antennas for testing the structures.

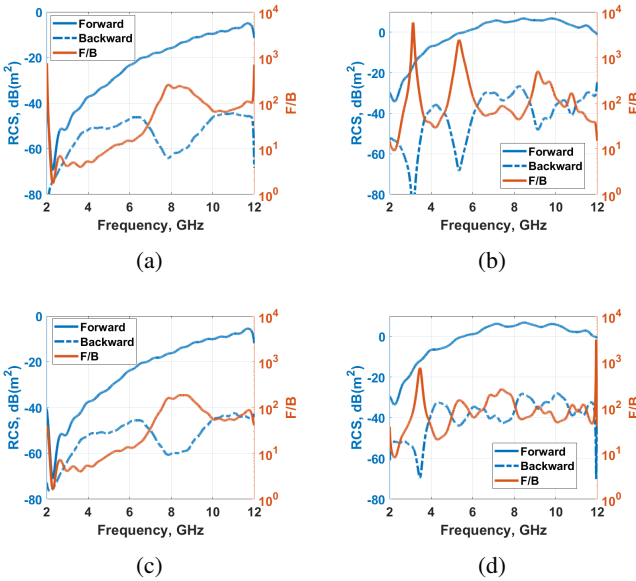


FIG. S6: (a)-(b) Experimentally obtained RCS spectra for the initial and optimized structures, respectively, including forward and backward scattering and their F/B ratio for the x-polarization; (c)-(d) the same plots but for the y-polarization.

Samples characterization

The experimental setup to characterize the samples is assembled in a certified anechoic chamber. It consists of two

horn antennas (NATO IDPH-2018, 2 GHz to 18 GHz) spaced 3 m apart, connected to a Keysight P9374A Network Analyzer (300 kHz–20 GHz) that can record S-matrix values in the complex representation for x- and y-polarizations, see Fig. S5c. Each measurement used network analyser settings of 5 dBm output power, 100 kHz input bandwidth, and 16001 points. Each sample was installed exactly at the midpoint between the antennas on a Styrofoam stage, which is transparent to microwave propagation. For quantitative measurements, a brass calibration disk of 10 cm diameter has been used. Time gating post-processing was applied to reduce the multipath impact further.

From the calculated RCS spectra of forward and backward scattering, along with their F/B ratio, shown in Fig. S6a-d, one can see a good agreement between the results and the simulations. As in the simulations, a strong minimum is observed in the backward scattering spectra of the optimized structure near the design frequency (Figs. S6b, and d). Therefore, the F/B ratios for the optimized structure are characterized by maxima (Fig. S7 – the red plots) compared with the initial structure (Fig. S7 – the blue plots). In the experimental study, a larger enhancement was achieved (~1300 for the x-polarization (Fig. S7c) at the frequency 3.13 GHz and 160 for the y-polarization at the frequency 3.47 GHz (Fig. S7d) compared to the simulation analysis in Fig. S3.

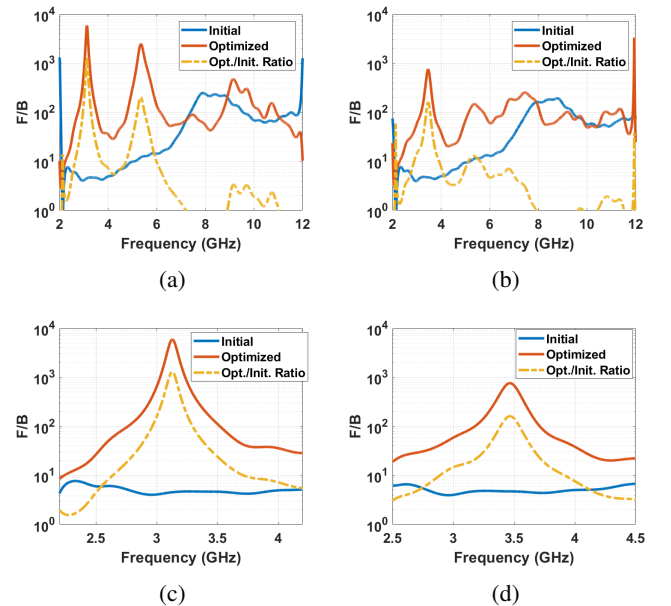


FIG. S7: Forward-to-backward (F/B) scattering for both experimental structures—initial (solid blue) and optimized (solid red)—and the forward-to-backward scattering ratio of the optimized to the initial cluster (dash-dotted), respectively, for the (a) x- and (b) y-polarization. A zoomed-in version of the same figure around the optimization frequency in (c) and (d), respectively.

Taking all these results, the experiments show that the methodology described in the main text can be used to optimize structures whose functionality is verifiable on experi-

mental grounds. The agreement between measurements and simulations reveals, moreover, the functionality of the design.